Aqueous Electrolytes Reinforced by Mg and Ca Ions for Highly Reversible Fe Metal Batteries

Jing Liu, Dengpan Dong, Alan Larrea Caro, Nicolai Sage Andreas, Zongjian Li, Yunan Qin, Dimitry Bedrov,* and Tao Gao*

Cite This: ACS Cent. Sci. 2022, 8, 729−740

Read Online

ACCESS | Metrics & More | Article Recommendations | SI Supporting Information

ABSTRACT: Iron (Fe) metal batteries, such as Fe-ion batteries and all Fe flow batteries, are promising energy storage technologies for grid applications due to the extremely low cost of Fe and Fe salts. Nonetheless, the cycle life of Fe metal batteries is poor primarily due to the low Coulombic efficiency of the Fe deposition/stripping reaction. Current aqueous electrolytes based on Fe chloride or sulfate salts can only operate at a Coulombic efficiency of <91% under mild operation conditions (<5 mA/cm^2), largely due to undesired hydrogen evolution reaction (HER). This work reports a series of novel Fe electrolytes, Fe electrolytes reinforced with Mg ions (FERMI) and Ca ions (FERCI), which have remarkably better

Coulombic efficiency, higher conductivity, and faster deposition/stripping kinetics. By the addition of 4.5 M MgCl$_2$ or CaCl$_2$ into the baseline FeCl$_2$ electrolyte, the Fe deposition/stripping efficiency can be significantly improved to 99.1%, which greatly boosts the cycling performance of Fe metal batteries in both half-cells and full-cells. Mechanistic studies reveal that the remarkably improved efficiency is due to a reduced amount of "dead Fe" as well as suppressed HER. By the combination of experiments and molecular dynamics and density functional theory computation, the electrolyte structure is revealed, and the mechanism for enhanced water reduction resistance is elucidated. These novel electrolytes not only enable a highly reversible Fe metal anode for low-cost energy storage technologies but also have the potential to address the HER side reaction problem in other electrochemical technologies based on aqueous electrolytes, such as CO$_2$ reduction, NH$_3$ synthesis, etc.
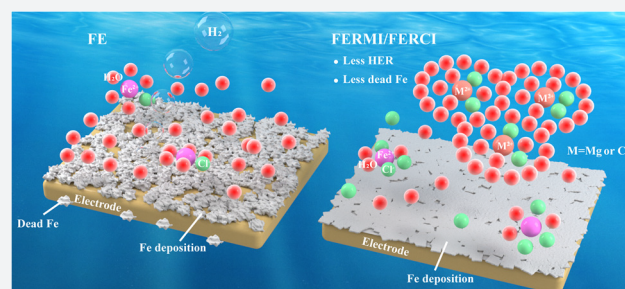
INTRODUCTION

Renewable energies, such as solar and wind, can decarbonize our energy generation and help to address the climate change grand challenge. However, their intermittent nature makes their integration into the grid difficult. Battery energy storage is a scalable technology that can buffer the mismatch between renewable electricity generation and grid electricity demand, but the high cost remains the main obstacle to its wide deployment. To be competitive for large-scale grid applications, battery technologies need to have a system cost of < $100/kWh and a levelized cost of storage (LCOS) of <$0.05/ kWh-cycle based on the U.S. Department of Energy's estimate.[1] To meet this goal, battery technologies need to be made of cheap and abundant materials, be easy to maintain, and have a long cycle life.

Among various battery technologies, aqueous iron (Fe) metal batteries are promising due to their low-cost potential.[2−6] Fe is the second most abundant metal in the earth's crust and is the most-produced metal commodity. Therefore, the cost of Fe ($60/ton) is much lower than any other metal used in rechargeable batteries, such as zinc ($2600/ton) and lithium ($16 500/ton).[6,7] In addition, Fe metal has a very high capacity (960 mAh/g and 7558 mAh/

cm^3) and outperforms zinc metal (820 mAh/g and 5854 mAh/ cm^3), the most popular metal anode used in aqueous batteries. Consequently, the material-level energy storage cost of an Fe metal battery is only $0.06/kWh (considering only the cost of the Fe anode), making it extremely promising for achieving the U.S. Department of Energy's cost target for large-scale grid energy storage.[1]

Motivated by this potential, many aqueous Fe metal batteries have been invented,[8] including Fe-ion batteries,[6,9] Fe−Ni batteries,[10] and all Fe redox flow batteries.[11] Despite these efforts, the promise of aqueous Fe metal batteries has not been realized due to their limited cycle life. Fe deposition/ stripping is the designed reaction that occurs at the anode in an aqueous Fe metal battery. However, the reversibility of this reaction is far from satisfactory for making a battery with a long lifespan. In acidic aqueous electrolytes, the hydrogen evolution
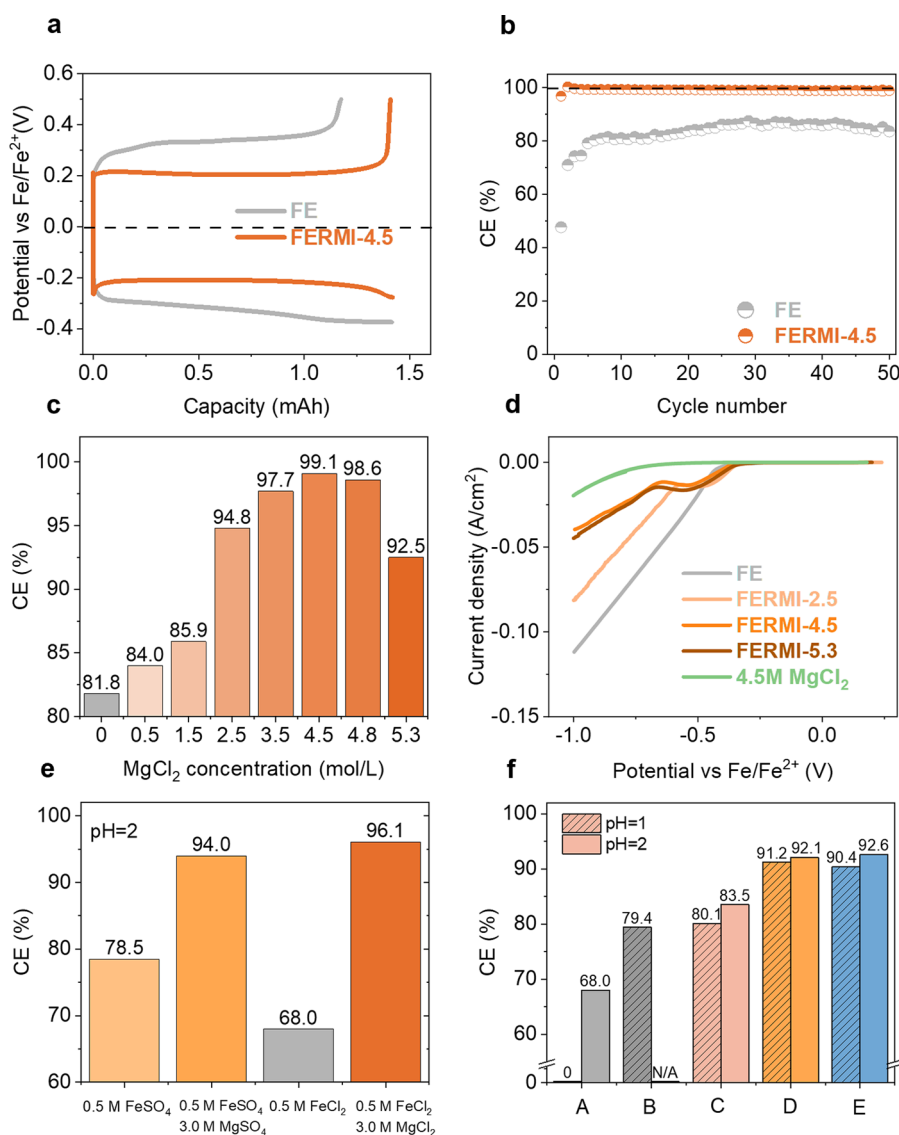
Figure 1. CE enhancement in FERMI (0.5 M FeCl$_2$ + x M MgCl$_2$) (a) Typical deposition/stripping voltage curves for FE (0.5 M FeCl$_2$) and FERMI-4.5 (0.5 M FeCl$_2$ + 4.5 M MgCl$_2$) in Cu|Fe two-electrode cells at 1 mA/cm^2 for 1 h. The data of the 20th cycle is shown here. (b) CE vs cycle number. (c) Average CE of FERMI-x without adjusting the pH. (d) Linear scan voltammetry of FE, 4.5 M MgCl$_2$, and FERMI-x electrolytes in the Cu|Fe|Fe three-electrode cell at 10 mV/s in the range of −1.0 to 0.2 V vs Fe reference electrode (RE). (e) Average CE of FE with Cl$^-$ and SO$_4^{2-}$, the corresponding FERMI at pH = 2. Here only 3.0 M Mg^{2+} is used since the solubility of MgSO$_4$ is 3.2 M. (f) Average CE of A (FE), B (FE + 2.5 M FeCl$_2$ (3.0 M FeCl$_2$)), C (FE + 5.0 M NaCl), D (FE + 2.5 M MgCl$_2$), and E (FE + 2.5 M CaCl$_2$) at different pH values; 3.0 M FeCl$_2$ has a pH = 1, and increasing its pH leads to precipitation of Fe(OH)$_2$. Therefore, the efficiency of 3.0 M FeCl$_2$ at pH = 2 is not available. The reason to choose pH = 1 and 2 for this comparison is that Fe^{2+} will precipitate as Fe(OH)$_2$ when the solution pH > 2.7 (the as-made 0.5 M FeCl$_2$ has a pH = 2.7), and Fe^{3+} will precipitate as Fe(OH)$_3$ when the solution pH > 1.2 (the as-made 0.5 M FeCl$_3$ has a pH = 1.2).[18] Note at pH = 1, there is no reversible Fe deposition/stripping in FE due to the strong acidity of the electrolyte (Figure S6), so the CE is zero.

reaction (HER) is thermodynamically more favorable than Fe deposition (HER: −0.12 V vs SHE at pH = 2; Fe deposition: −0.44 V vs SHE). Consequently, HER competes with Fe deposition during the charging of an Fe battery. Unlike zinc metal which has a high overpotential for HER, Fe is known as a catalyst for HER;[12] therefore, HER kinetics are very facile on the deposited Fe. As a result, the Coulombic efficiency (CE) of Fe deposition/stripping is less than 91% in sulfate solutions[8,11] and less than 87% in chloride solutions[13] under mild deposition currents (<5 mA/cm^2). Such low CE leads to gas generation and electrolyte pH increase during battery cycling, which further causes the hydrolysis of Fe$^{2+/3+}$, precipitation of ferrous/ferric hydroxide, and battery performance degradation. Previous studies have shown that increasing the electrolyte pH,

adding ascorbic acid buffer, chloride, or Cd additive, and raising the electrolyte temperature can increase CE.[13,14] However, the best CE reported so far is still not sufficient to build a long cycle life Fe battery. Electrolytes capable of depositing/stripping Fe metal with high efficiency (>99%) are in urgent demand for the development of long-life aqueous Fe metal batteries.

In this work, we report a series of novel aqueous electrolytes that can deposit/strip Fe metal at an efficiency of up to 99.1%, which is the best efficiency to our knowledge. The electrolytes, called Fe electrolyte reinforced with magnesium ions (FERMI) and Fe electrolyte reinforced with calcium ions (FERCI), can be simply made by adding the cheap and abundant MgCl$_2$ and CaCl$_2$ salts into the baseline FeCl$_2$ electrolyte. The electro-
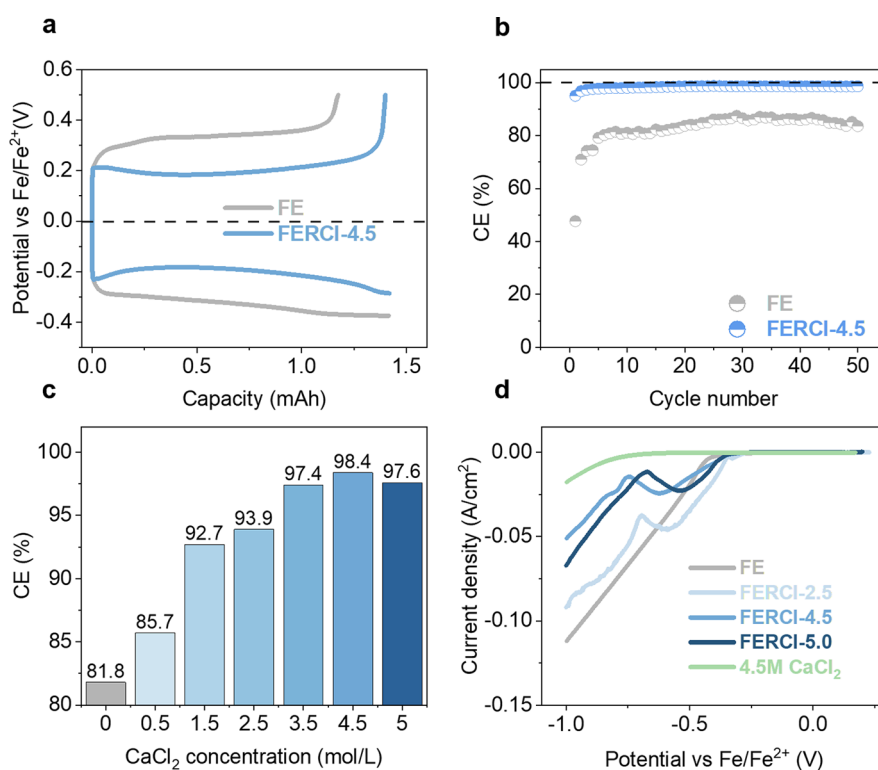
Figure 2. Similar CE enhancement in FERCI (0.5 M $FeCl_2$ + xM $CaCl_2$). (a) Typical deposition/stripping voltage curves for FE and FERCI-4.5 in Cu|Fe two-electrode cells at 1 mA/cm^2 for 1 h. The data of the 20th cycle is shown here. (b) Coulombic efficiency vs cycle number. (c) Average CE of Fe electrolytes at different $CaCl_2$ concentrations. (d) Linear scan voltammetry of FE, 4.5 M $CaCl_2$, and FERCI-x electrolyte in the Cu|Fe|Fe three-electrode cell at 10 mV/s in the range of -1.0 to 0.2 V vs Fe RE.

chemical performance of the electrolytes is presented, and a combined experimental and computational study is performed to reveal the underlying mechanisms of the remarkable performance.

■ RESULTS

Pure Fe electrolyte is made by dissolving the Fe salt into deionized water, and the FERMI is made by dissolving $MgCl_2$ into Fe electrolyte. We chose 0.5 M $FeCl_2$ (FE) as the baseline for comparing the Fe deposition/stripping efficiency and other performances of Fe electrolytes. Baseline Fe electrolytes added with different concentrations of magnesium (Mg) ions/calcium (Ca) ions are denoted as FERMI-x/FERCI-x, in which x is the molarity of the Mg/Ca ion. Fe deposition/stripping experiments were performed in Cu|Fe two-electrode cells, in which a Cu foil is the substrate for Fe deposition, and an Fe foil is the Fe source. Since the standard reduction potentials of Mg^{2+}, Ca^{2+}, and Fe^{2+} are -2.37, -2.87, and -0.44 V vs SHE, respectively, Mg/Ca deposition is not likely to happen at the potential where Fe deposition occurs (>-0.5 V vs Fe/Fe^{2+}). This is confirmed by the X-ray diffraction (XRD) pattern/energy dispersive spectroscopy (EDS) results (Figure 3). Typical potential curves for Fe deposition/stripping in FE and FERMI-4.5 are shown in Figure 1a, in which the negative potential corresponds to Fe deposition, and the positive potential corresponds to Fe stripping. An upper cutoff of 0.5 V vs Fe/Fe^{2+} is chosen during stripping to avoid the oxidation of the Cu substrate ($Cu - 2e^- = Cu^{2+}$) because the oxidation potential of Cu is 0.78 V vs Fe/Fe^{2+} under standard conditions and >0.5 V vs Fe/Fe^{2+} in our studied electrolytes (Figure S1). The CE is calculated by dividing the

oxidation capacity with respect to the reduction capacity. FERMI-4.5 shows not only improved CE compared to FE ($99.1 \pm 0.2\%$ vs $81.8 \pm 7.2\%$) but also increased conductivity (86.0 vs 66.7 mS/cm, Figure S2) and better deposition/stripping kinetics (total overpotential: 420 vs 900 mV). The potential curves during repeated deposition/stripping cycling are shown in Figure S3, and the CEs are shown in Figure 1b, in which an initial activation process is seen for both electrolytes. The initial cycle CE of FE is only 47.7%, whereas the initial cycle CE of FERMI is 96.8%. The FE reaches a stable CE of ~82% after 10 cycles, whereas FERMI reaches a stable CE of 99.1% after only four cycles. This remarkably increased efficiency, 99.1%, is the best reported efficiency for Fe deposition/stripping in aqueous electrolytes to our knowledge.

To investigate how $MgCl_2$ affects the Fe deposition/stripping CE, the average CEs of FERMI at different concentrations of $MgCl_2$ (C_{MgCl2}) are compared in Figure 1c. The average CE first increases with C_{MgCl2} and then starts to decrease after reaching a peak. A maximum CE, 99.1%, is achieved in FERMI-4.5. The non-monotonic dependence of CE on C_{MgCl2} could be related to the non-monotonic conductivity change (Figure S2). Higher salt concentration leads to higher viscosity and lower conductivity. The associated larger overpotential leads to early termination of the stripping process, therefore lowering the CE. The low CE of FE is in large part due to the competing HER during Fe deposition, as many gas bubbles were seen on the surface of the deposited Fe during reduction. The enhanced CE in FERMI is likely due to the suppressed HER since fewer gas bubbles were seen. To confirm this, linear scanning voltammetry (LSV) tests in a Cu|Fe|Fe three-electrode cell were performed in a voltage range of 0.2 to -1.0 V in FE, FERMI, and 4.5 M $MgCl_2$ (Figure 1d). In
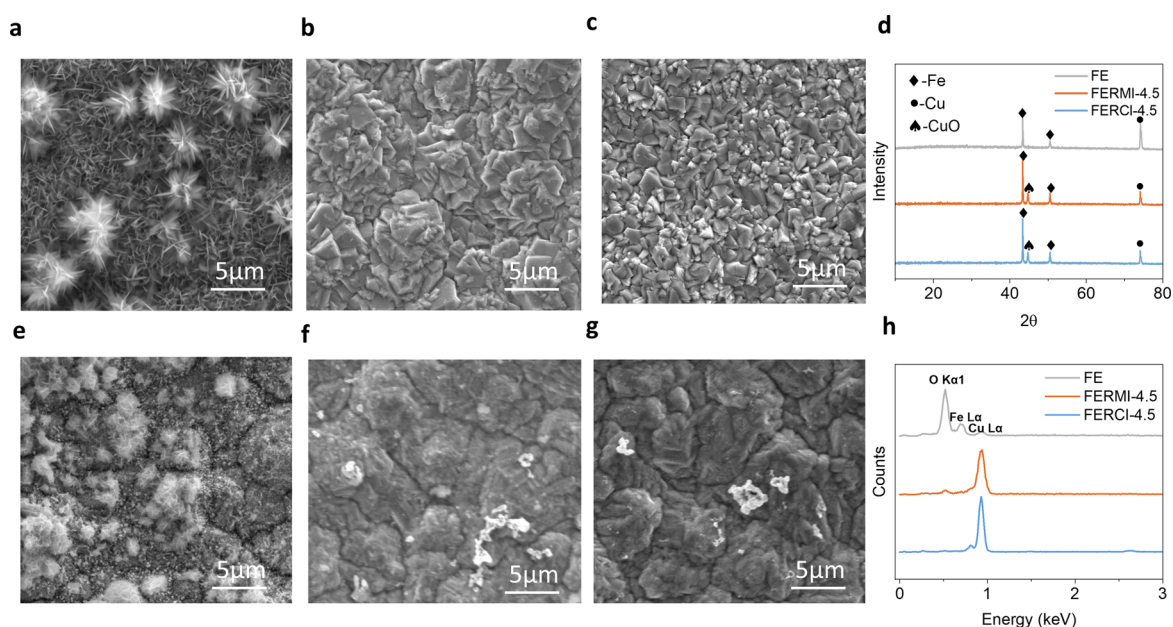
Figure 3. Characterization of the deposits in FE, FERMI-4.5, and FERCI-4.5. SEM of the deposits in (a) FE, (b) FERMI-4.5, and (c) FERCI-4.5 after the first deposition. (d) XRD of the deposits in FE, FERMI-4.5, and FERCI-4.5 after the first deposition. SEM of the Cu substrates in (e) FE, (f) FERMI-4.5, and (g) FERCI-4.5 after the first stripping. (h) EDS of the Cu substrates in FE, FERMI-4.5, and FERCI-4.5 after the first stripping.

FE, the peak for Fe^{2+} reduction is not visible due to the strong HER. For FERMI-2.5, the Fe^{2+} reduction peak becomes visible, and the HER current reduces. For FERMI-4.5, the HER current further decreases. The HER current in FERMI-4.5 is only $-0.039 A/cm^2$ at -1.0 V, which is three times smaller than that in FE, suggesting the HER is suppressed in FERMI. For FERMI-5.3, the HER current slightly increases compared to FERMI-4.5. The dependence of HER suppression on Mg^{2+} concentration is consistent with the observed CE, confirming that the suppression of the HER is a main reason for the increased CE in FERMI. LSV results in an anodic scan showing that in the FERMI/FERCI, the Fe^{2+}/Fe^{3+} redox peak has less overlap with the oxidation of the chloride solution than in the FE (Figure S4), which is beneficial for achieving high cathode CE in an all Fe flow battery.

When $MgCl_2$ is dissolved into FE, the pH of the solution slightly increases (pH of FE = 2.7, pH of FERMI-4.5 = 4.1) (Figure S5), which can mitigate the HER due to the reduced proton concentration. In addition, the increased concentration of Cl^- can also suppress the HER[15] due to its preferential adsorption to the electrode surface.[16,17] To examine only the effect of Mg^{2+}, two additional experiments were performed. First, FE made with $FeCl_2$ and $FeSO_4$ is compared with the FERMI with the same anion at the same pH (pH = 2) (Figure 1e). A clear increase in CE (28.1% for Cl^-, 15.5% for SO_4^{2-}) is observed when 3.0 M Mg salts are added into FE, irrespective of the anion. This result suggests that the effect of Cl^- on the CE is likely to be secondary. Second, Fe electrolytes with the same amount of Cl^- but distinct types of cations (Fe^{2+}, Na^+, and Mg^{2+}) are compared at the same pH (Figure 1f). We choose a total Cl^- concentration of 6.0 M to compare the effect of different cations because the solubility of NaCl is 5.5 M and the solubility of $FeCl_2$ is 3.57 M. At pH = 1, the CE of FE is zero because at such a high H^+/Fe^{2+} molar ratio (0.1 M/ 0.5 M = 0.2), Fe^{2+} reduction fails to compete with H^+ reduction, so the HER dominates. The CE increases to 79.4% if an additional 2.5 M $FeCl_2$ is added into the FE (3.0 M

$FeCl_2$). When comparing the electrolytes with the same Cl^- concentration (6.0 M) but different cations, electrolytes containing Mg^{2+} show better CE than those containing Na^+ and Fe^{2+} at both pH = 1 and 2. As for the pH effect, electrolytes containing both Mg^{2+} and Na^+ show only a slight increase (0.9−3.4%) in CE when the pH is increased from 1 to 2. In summary, these results demonstrate that (1) Mg^{2+} can enhance the CE regardless of the type of anion and electrolyte pH and (2) the significant increase of the CE in FERMI is to be primarily due to the presence of Mg^{2+} whereas pH and Cl^- only play minor roles.

A similar enhancement of Fe deposition/stripping efficiency can also be achieved with Ca^{2+}. The typical potential curves for Fe deposition/stripping in FE and FERCI are compared in Figure 2a, and the CEs during cycling are compared in Figure 2b. Like FERMI, the FERCI-4.5 shows a stable CE of 98.4 ± 0.48% after the initial activation cycles. The CE of FERCI at different Ca^{2+} concentrations is shown in Figure 2c, and a maximum CE of 98.4% is achieved for FERCI-4.5. The LSV results of FE, FERCI, and 4.5 M $CaCl_2$ are compared in Figure 2d. FERCI and 4.5 M $CaCl_2$ show a similar HER suppression effect: the peak HER current at -1.0 V drops from -0.11 A/cm^2 in FE to $-0.05 A/cm^2$ in FERCI-4.5. In addition, the dependence of HER suppression on the Ca^{2+} concentration is consistent with the CE's dependence. These results demonstrate that Ca^{2+} can also improve Fe deposition/stripping efficiency by suppressing the HER. To confirm the enhancement of the CE in FERMI and FERCI, the CE for Fe deposition/stripping is measured with another method (Figure S7).[19] As can be seen, the efficiency increases significantly after the addition of Ca^{2+} or Mg^{2+}, which validates the enhancement of the CE regardless of the methods used for measuring the efficiency.

To further understand the enhanced CE in FERMI and FERCI, scanning electron microscope (SEM) images of Fe deposits after the first deposition in FE, FERMI-4.5, and FERCI-4.5 are compared in Figure 3a−c and Figure S8. The
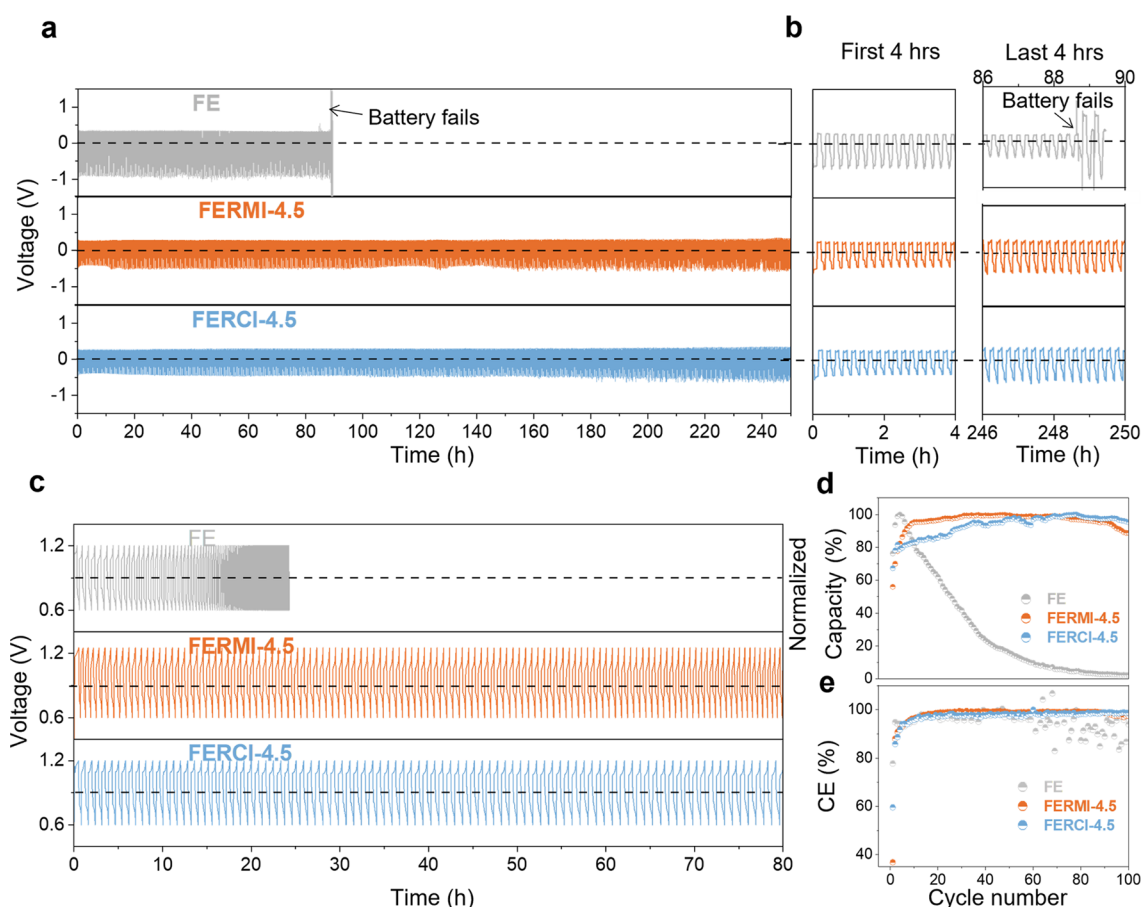
Figure 4. Cycling performance of Fe|Fe symmetric cells and LiFePO$_4$|Fe full-cells in FE, FERMI-4.5, and FERCI-4.5. (a) Voltage vs cycling time of Fe|Fe symmetric cells with FE, FERMI-4.5, and FERCI-4.5. Cycling condition: 1.0 mA/cm^2. (b) The first and last 4 h of the cycling results. (c) Voltage vs cycling time of LiFePO$_4$|Fe cells with FE, FERMI-4.5, and FERCI-4.5. Cycling condition: 1.0 mA/cm^2. (d) Normalized capacity and (e) CE vs cycle number of LiFePO$_4$|Fe cells with FE, FERMI-4.5, and FERCI-4.5.

deposits in FE are a loosely connected flowerlike assembly of nanosheets (Figure 3a, Figure S8), whereas the deposits in FERMI and FERCI are compactly stacked micrometer-sized and submicrometer-sized particles. Obviously, the deposits in FE have a larger surface area to volume ratio than those in FERMI and FERCI, which provide more sites for HER to occur. XRD of the deposits in these electrolytes is shown in Figure 3d. Strong Fe signals can be seen in all of them, suggesting the excellent crystallinity of Fe deposits. The presence of CuO and weakened Cu signals in FERMI-4.5 and FERCI-4.5 is likely a result of the chemical corrosion of the Cu substrates by Cl$^-$. The chemical corrosion of Cu in chlorine solution is well-known[20] and can be described by Cu + H$^+$ + 2Cl$^-$ = 0.5H$_2$ + CuCl$_2^-$. Note the electrochemical oxidation of Cu cannot explain this phenomenon because the working electrode is in a reductive environment during the Fe depositing process. The chemical corrosion does not intervene in the calculation of the Coulombic efficiency because the electron transferred from Cu to H$^+$ does not go through the external circuit; therefore, it is not counted by the potentiostat during the Fe deposition/stripping experiment. SEM images of the Cu substrates after the first stripping are compared in Figure 3e−g and Figure S9. Many fluffy clusters of a few micrometers in size and large quantities of nanoparticles exist on the surface of the Cu substrate in FE. Its EDS shows a strong signal of Fe Lα (Figure 3h, Table S2), suggesting these clusters and nanoparticles are unreacted Fe during the

stripping process, i.e., "dead Fe". Such "dead metal" is commonly observed in the stripping of electrochemically deposited metals, such as Li and Na.[21] It occurs when metal deposits are electrically isolated from the substrate during the stripping process, which is common for deposits with skinny morphology.[22] The weak signal of Cu Lα indicates that the dead Fe covers most of the Cu substrate. The strong O Kα1 signal is likely due to the oxidation of the dead Fe during the sample preparation. In stark contrast, far less dead Fe is observed on the Cu substrates in FERMI-4.5 and FERCI-4.5, and EDS shows a strong sign of Cu Lα but no clear sign of Fe Lα, confirming there is little dead Fe on the Cu substrates. The strong signal of Cu and the absence of anion signals (Cl and O) also suggest that no solid electrolyte interface (SEI) forms on the Cu substrate since SEI should contain compounds of the corresponding ions in the electrolyte. Mg and Ca or their oxides/hydroxides are not observed in either the XRD or EDS results, confirming that Mg/Ca deposition does not occur in these electrolytes. In summary, these results demonstrate (1) only Fe deposition occurs in FERMI and FERCI, (2) they promote the growth of large and compact Fe deposits, and (3) they reduce the amount of dead Fe during the stripping process. The better Fe deposits morphology and less dead Fe in FERMI and FERCI are other reasons for the better Fe deposition/stripping efficiency.

To demonstrate how the Fe deposition/stripping efficiency affects the Fe metal battery's cycle life, cycling experiments
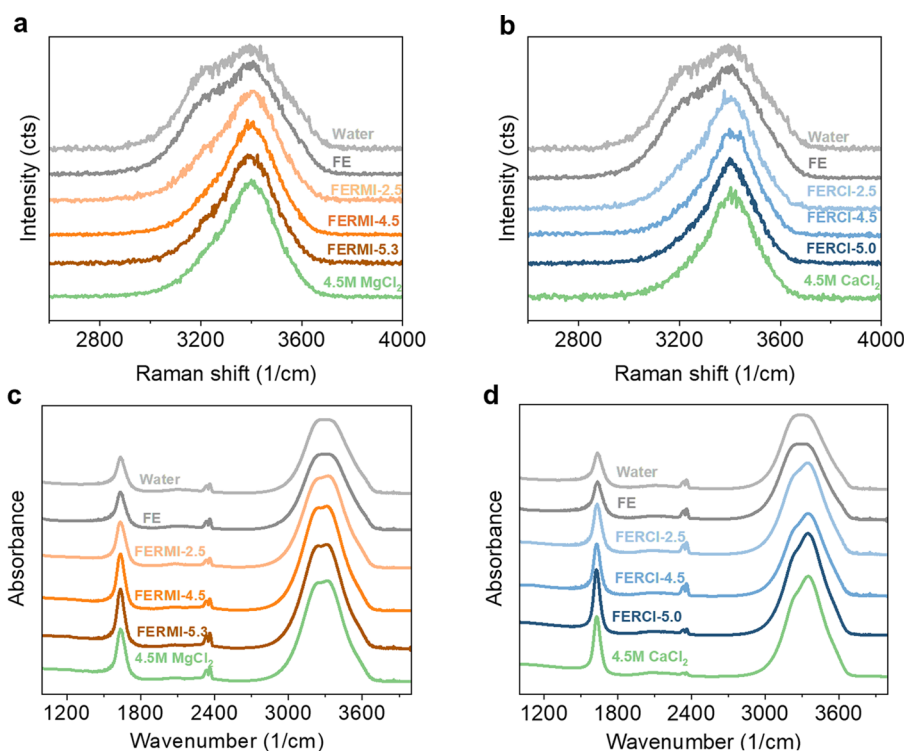
Figure 5. Raman spectra and FT-IR Raman spectra of (a) water, FE, FERMI-*x*, and 4.5 M MgCl$_2$ and (b) water, FE, FERCI-*x*, and 4.5 M CaCl$_2$. FT-IR of (c) water, FE, FERMI-*x*, and 4.5 M MgCl$_2$ and (d) water, FE, FERCI-*x*, and 4.5 M CaCl$_2$.

were performed with Fe|Fe symmetrical cells and LiFePO$_4$|Fe full-cells (Figure 4). During cycling, side reactions, including HER, will change the electrolyte's chemistry over time and eventually fail the cell. The Fe|Fe symmetrical cells were cycled by charging for 0.1 h and then discharging for another 0.1 h both at 1.0 mA/cm^2 without constraining the voltage. The voltage profiles during cycling are compared in Figure 4a and b. The cells with FE can work for 88.5 h, and then the cells fail, which is signaled by a sudden increase in voltage caused by an increase in the internal cell resistance from 0.86 to 17.1 Ω (Figure S10). The failed coin cells swelled, indicating the generation of a large amount of gas inside the cell (Figure S11). After the failed cells were assembled, the electrolyte almost dried out, and green precipitate could be found on the spacer (Figure S12). These results suggest the internal resistance increase can be attributed to the following reasons: (1) the generated gas bubbles block the ion transport pathway between the working and counter electrodes, (2) HER consumes water and leads to an increase in electrolyte viscosity, and (3) the pH increase and the precipitation of Fe salts. In contrast, the cell with FERMI-4.5 and FERCI-4.5 can work for >250 h with no significant increase in voltage. Similar results were observed in Cu|Fe cells as well (Figure S13). To further demonstrate how the improved Fe anode CE affects the Fe metal battery's cycle life, LiFePO$_4$|Fe full-cells with FE, FERMI-4.5, and FERCI-4.5 are assembled and tested. The cells were charged/discharged at 1.0 mA/cm^2 in the voltage range of 0.60−1.25 V. The voltage profiles during cycling are compared in Figure 4c. The cell with FE fails rapidly within the first 20 h, whereas the cells with FERMI-4.5 and FERCI-4.5 can operate for over 80 h without clear signs of degradation. The normalized capacity and CE are compared in Figure 4d and e, respectively. All cells undergo an activation process before reaching the maximum capacity, which could be

attributed to the slow wetting of aqueous electrolytes to the graphite felt current collector. The cell with FE fades rapidly and loses 97.7% of the capacity at the 100th cycle, whereas cells with FERMI-4.5 and FERCI-4.5 show very stable cycling and lose only 11.2% and 4.67% of the capacity at the 100th cycle. Meanwhile, the cell with FE shows an average CE of 95.2%, whereas the cells with FERMI and FERCI show average CEs of 97.7% and 97.2%, respectively. The cycling performances and CEs of LiFePO$_4$|Fe full-cells in FE, FERMI-4.5, and FERCI-4.5 with no Li salts are given in Figure S14. Cells with FERMI-4.5 and FERCI-4.5 show much more stable cycling than cells with FE, which is consistent with Figure 4d and e. In summary, these results demonstrate that the enhanced Fe anode efficiency in FERMI and FERCI can significantly boost the cycling performance of Fe metal batteries in both half-cells and full-cells.

To understand the effect of Mg^{2+} and Ca^{2+} on the Fe electrolytes, Raman and Fourier transform infrared (FTIR) spectra of FE, FERMI, and FERCI are collected and compared (Figure 5). In aqueous electrolytes, the water interacts strongly with the ions by electrostatic interaction, H-bonding, or charge transfer.[23] The preferred orientation, H-bonding, and vibrational dynamics of water in the hydration shell are very different from those of the bulk water. Water can form a maximum of four H-bonds with its neighboring water molecules by donating two protons and accepting two protons to the lone pair of electrons on oxygen. Based on how strongly a water molecule participates in H-bond formation, four types of water are possible at ambient temperature. In the order of decreasing number of H-bonds, they are DDAA, DDA, DAA, and DA, in which D refers to water molecules donating a proton, and A refers to water molecules accepting a proton (i.e., DDA means double donor−single acceptor).[24] In the Raman spectra of pure water, the OH symmetric stretch region
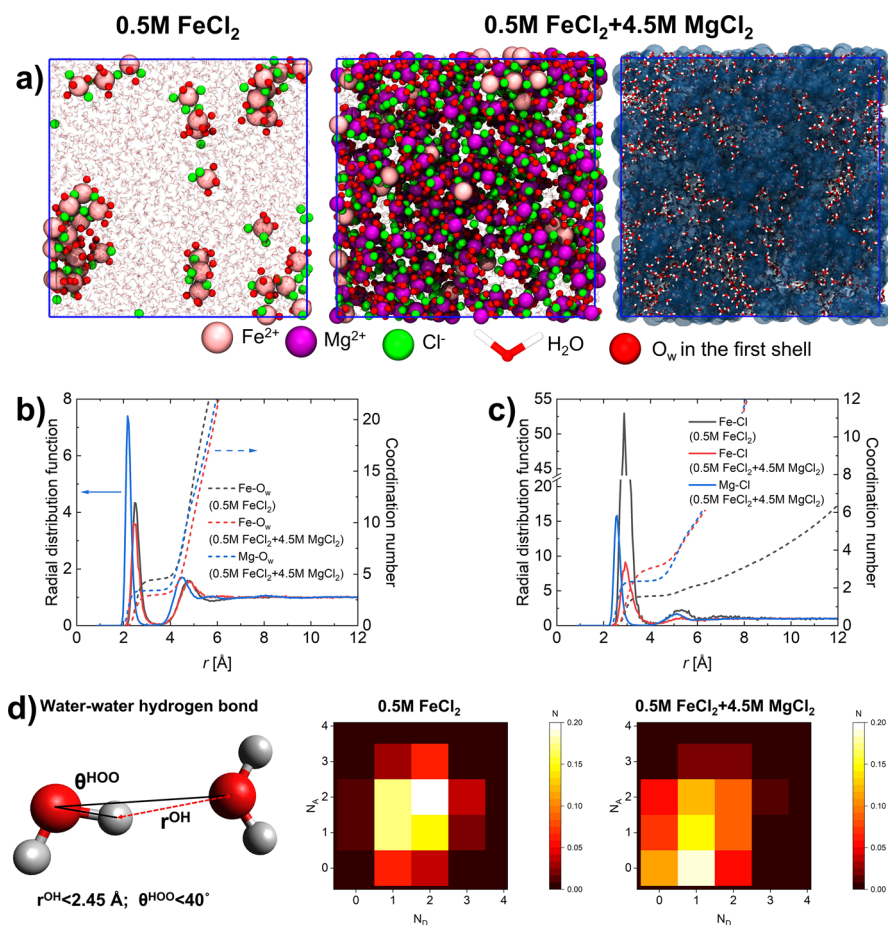
Figure 6. Electrolyte structure from MD simulations: (a) snapshots of 0.5 M $FeCl_2$ (left) and 0.5 M $FeCl_2$ + 4.5 M $MgCl_2$ (right) from MD simulations. Ions are highlighted as spheres. O_w atoms in the first coordination shell of the cation are highlighted as red spheres. Snapshot on the far-right highlights the water distribution in which all ions are shown as the semitransparent blue background. (b) The cation–O_w radial distribution function (left y-axis) and the corresponding coordination number (right y-axis). (c) The cation–anion radial distribution function (left y-axis) and the corresponding coordination number (right y-axis). (d) Hydrogen bonding. The water–water H-bond is determined by three criteria, i.e., $r^{OH} < 2.45$ Å, $\theta^{HOO} < 40°$, and two water molecules located inside the first coordination shell. The colored pixels illustrate the probability of water molecules participating in different numbers and types of H-bonds. N_A is the number of H-bonds water participates in by accepting a proton, and N_D is the number of H-bonds water participants in by donating a proton.

has a broad peak with three bands at ∼3200, ∼3400, and ∼3600 cm^{-1}, which can be assigned to DDAA water, DA water, and DDA water, respectively.[24] In FE, the molar ratio of H_2O to Fe^{2+} is 105 (Table S1). Since Fe^{2+} prefers octahedral coordination, there are at most six water molecules in its hydration shell so that most water molecules exist in the bulk. Therefore, the Raman spectroscopy of FE is close to that of pure water. Nonetheless, the water structure changes significantly after the addition of Mg^{2+} or Ca^{2+}. Due to the high charge density of Mg^{2+} and Ca^{2+}, its influence on water structure and dynamics extends beyond the first hydration shell. In dilute electrolytes, both Mg^{2+} and Ca^{2+} immobilize ∼20 water molecules,[25] forming two hydration shells around them, with the first hydration shell containing six water molecules for Mg^{2+} and six–nine water molecules for Ca^{2+}.[26] Upon an increase of the concentration of Mg^{2+}/Ca^{2+}, the number of water molecules in the hydration shell of Mg^{2+}/Ca^{2+} increases proportionally up to a certain concentration (2.0 M for Mg^{2+}, in which the molar ratio of water and Mg^{2+} is ∼25).[27] With further increase of the concentration of Mg^{2+}/Ca^{2+}, solvent-separated ion pairs (2SIP) or even solvent-shared ion pairs (SIP) can form. At 4.5 M Mg^{2+}/Ca^{2+}, the molar ratio of H_2O to Mg^{2+}/Ca^{2+} is ∼10, suggesting that all water

molecules exist in the hydration shells of Mg^{2+}/Ca^{2+}, and a portion of this hydration shell water is shared with Cl^-. In the hydration shells, the O atoms of water point toward Mg^{2+}/Ca^{2+}, and H atoms point away. For water molecules shared with Cl^-, their H atoms point toward the Cl^-. Due to this orientation preference and geometric constraint, hydration shell water forms fewer H-bonds than bulk water. Therefore, the presence of a large amount of Mg^{2+}/Ca^{2+} disrupts the water structure and eliminates strongly hydrogen-bonded water. Previous studies show that the ∼3600 cm^{-1} band and ∼3200 cm^{-1} band in the Raman spectrum weaken as 1.0−2.0 M Mg^{2+}/Ca^{2+} is added.[27,28] Here in our results, a similar weakening effect is observed at 2.5 M of Mg^{2+}/Ca^{2+}. These two bands completely disappear at 4.5 M Mg^{2+}/Ca^{2+}, and further increase of the Mg^{2+}/Ca^{2+} concentration results in no observable change (Figure 5). These results indicate that the addition of 4.5 M Mg^{2+}/Ca^{2+} eliminates DDA water and DDAA water, which leads to fewer H-bonds per water. Similar suppression of the ∼3200 cm^{-1} band is also observed in the OH-stretching region of the FT-IR spectra of FERMI and FERCI. The intensity of the O−H−O bending vibration peak at 1600 cm^{-1} grows with increasing Mg^{2+}/Ca^{2+} concentration, also indicating the weakening of the H-bond. In addition to the

change in water structure, the hydration shell of Fe^{2+} also changes after adding Mg^{2+}/Ca^{2+}. In FE, Fe^{2+} mostly exists as $[Fe(H_2O)_6]^{2+}$ in an octahedral configuration.[29] Given that the ratio of Fe^{2+}/H_2O decreases in FERMI and FERCI, the solvation shell of Fe^{2+} will have fewer water molecules and more Cl^-. A similar effect has been observed for Zn^{2+} when less water is available.[30] The computational study below will elucidate this change in the Fe^{2+} solvation shell.

To further understand the electrolyte structure, atomistic molecular dynamics (MD) simulations using the polarizable force field (APPLE&P)[31,32] were performed for FE (0.5 M $FeCl_2$) and FERMI-4.5 (0.5 M $FeCl_2$ + 4.5 M $MgCl_2$) at room temperature. The simulations contained 4000 water molecules and the corresponding number of ions. The snapshots in Figure 6a illustrate the structure of both electrolytes. In 0.5 M $FeCl_2$, most water molecules do not interact with ions. While the ion can form small clusters, they are homogeneously distributed throughout the system. In 0.5 M $FeCl_2$ + 4.5 M $MgCl_2$, the electrolyte structure and distribution of water change significantly. Figure 6a shows that ions now form a continuous phase, and the water structure is significantly perturbed. The cation−oxygen of water (O_w) radial distribution functions (RDFs) with corresponding apparent coordination numbers are shown in Figure 6b as a function of shell radius, and the cation−anion RDFs are shown in Figure 6c. The strong first peak in the RDF defines the first solvation shell (3.40 Å for Fe^{2+} and 3.15 Å for Mg^{2+}). The shorter $Mg-O_w$ distances and stronger first and second solvation shell peaks of Mg^{2+} indicate that water molecules are tightly bound to Mg^{2+} due to stronger charge localization. The shorter $Mg-Cl$ distance than $Fe-Cl$ distance reveals a closer packing between Mg^{2+} and Cl^- than for the Fe^{2+}. The numbers of water molecules and Cl^- in the solvation shell of Fe^{2+} and Mg^{2+} are given in Table S3. The first solvation shell of Fe^{2+} contains an average of 4.5 water molecules and 1.6 Cl^- in 0.5 M $FeCl_2$. After the addition of 4.5 M $MgCl_2$, the solvation shell of Fe^{2+} changes to 3.0 water molecules and 3.1 Cl^-. The first solvation shell of Mg^{2+} contains an average of 3.4 water molecules and 2.4 Cl^-.

Analysis of water−water hydrogen bonding (Figure 6d and Table 1) shows that in 0.5 M $FeCl_2$, water molecules on

Table 1. Number of H-bonds per Water Molecule and the Corresponding Probability

Number of H-bonds / System	4 and 4+	3	2	1	0
0.5 M $FeCl_2$	0.366	0.321	0.231	0.075	0.0
0.5 M $FeCl_2$ + 4.5 M $MgCl_2$	0.200	0.234	0.240	0.243	0.083

average have 3.2 H-bonds, with 36.6% of them participating in four or more H-bonds (donor and acceptor combined), 32.1% participating in three H-bonds, 23.1% participating in two H-bonds, and only a small fraction participating in one or no H-bond. The addition of 4.5 M $MgCl_2$ significantly perturbs the H-bonding network between water molecules, as the average number of H-bonds per water molecule reduces to 2.2 and the fraction of water molecules that participate in four or more

hydrogen bonds drops to 20.0%. Instead, the fraction of water molecules participating only in one or no H-bond increases to more than 32%. Note, in molecular simulations, depending on the geometric definition of the H-bond, molecules that have more than four H-bonds are possible. This is because no matter what definition one chooses, there will always be some molecules in transition between two H-bonds where both bonds will formally fall within the boundary of the definition and be counted.[33] For the same reason, the computed average number of H-bonds per water molecule will be higher than in experiments. In addition to the reduced number of H-bonds per water, the averaged H-bond length increases from 2.024 to 2.085 Å after the addition of $MgCl_2$, indicating the weakening of the H-bond strength.

In summary, the simulations show that the electrolyte structure undergoes several major changes after the addition of 4.5 M $MgCl_2$: (1) Mg^{2+} is strongly bound with water molecules; (2) the number of H-bonds per water molecule reduces from 3.2 to 2.2; (3) the number of water molecules in the first solvation shell of Fe^{2+} reduces from 4.5 to 3.0; and (4) the average length of H-bonds increases. These changes are consistent with our analysis based on the Raman spectroscopy and FT-IR results. With fewer H-bonds per water molecule and longer H-bonds, the water O−H covalent bond becomes shorter and stiffer, therefore making hydrogen evolution more difficult.[34,35] In addition, the reduced number of water molecules in the hydration shell of Fe^{2+} makes water reduction more difficult because the likelihood of water reduction decreases when Fe^{2+} is brought to the vicinity of the electrode surface for the deposition reaction.[36,37]

To further elucidate the water molecule's enhanced resistance to the reduction in FERMI-4.5, density functional theory (DFT) calculations were performed to calculate the reduction potentials of water in the solvation shell of different cations and water with different numbers of H-bonds. First, we investigated the reduction of MCl_2 clusters (M = Fe^{2+}, Mg^{2+}, and Ca^{2+}) hydrated with five water molecules and one hydronium ion. The latter is introduced due to the acidic environment of the investigated electrolytes. Considering the first-electron reduction reaction generating the hydrogen radical as the rate-limiting step, the calculation of absolute reduction potential has been achieved by using a traditional Born−Harber cycle (Figure 7a and b), which is widely used in the calculations of redox reactions for battery electrolytes and electrochemical reactions in aqueous phases.[38−40] When Fe^{2+} is the cation, the reduction potential is −0.302 V vs Fe/Fe^{2+}, but the reduction potential reduces to −0.999 and −0.723 V when the central cation is replaced with Mg^{2+} or Ca^{2+}, respectively. Next, we investigated the influence of the number of H-bonds per water molecule on its reduction. Our experiment and MD simulation both show that the average number of H-bonds per water decreases after the addition of 4.5 M $MgCl_2$. To examine how the number of explicit H-bonds that water molecules participate in affects its reduction potential, we compared the reduction of water molecules with four and two H-bonds. A water molecule with four H-bonds (2A2D) is represented by the central H_2O in a five-H_2O cluster (Figure 7c). Water with two H-bonds is represented by the central H_2O in a three-H_2O cluster. Since there are three different isomers of three-H_2O clusters with 1A1D, 0A2D, and 2A0D H-bonds, the reduction potentials of the central water in them were computed respectively to investigate how the H-bond type influences the reduction potential. Using the
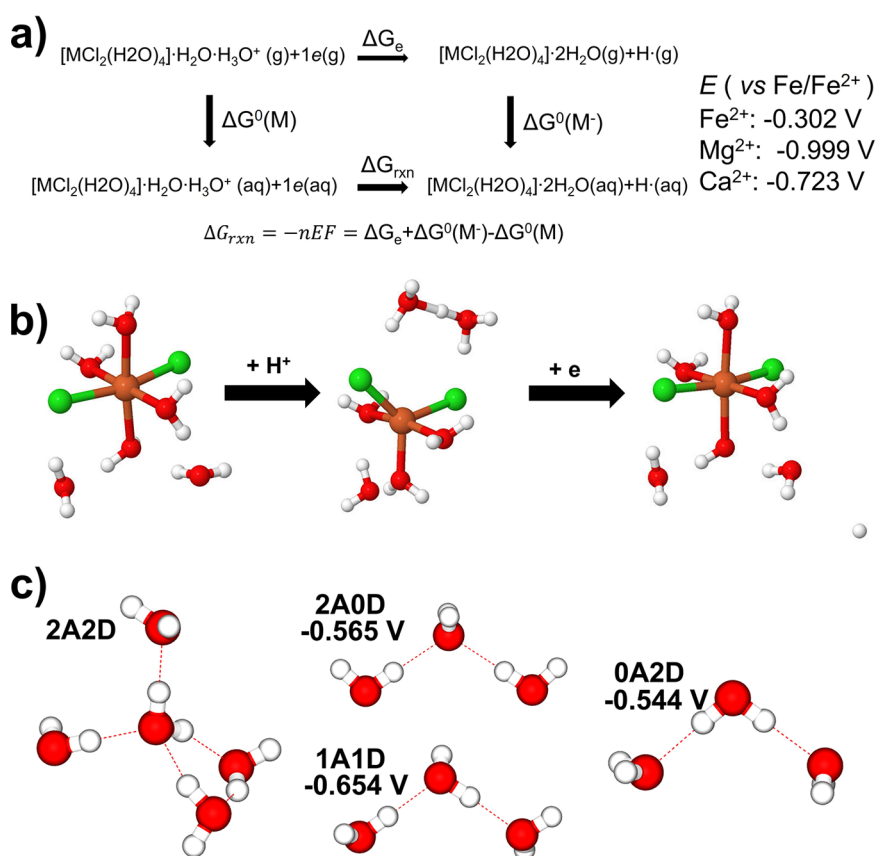
Figure 7. Electrochemical reduction of H_2O. (a) The calculation of the electrochemical reduction potentials of MCl_2 clusters (M = Fe^{2+}, Mg^{2+}, and Ca^{2+}) hydrated with five water molecules and one hydronium ion. (b) Geometries of the hydrated $FeCl_2$ cluster investigated for the reduction reaction. (c) Geometries and reduction potentials of water molecules in a cluster with different numbers and types of H-bonds. The reduction potential of three-H_2O clusters is given relative to the five-H_2O clusters.
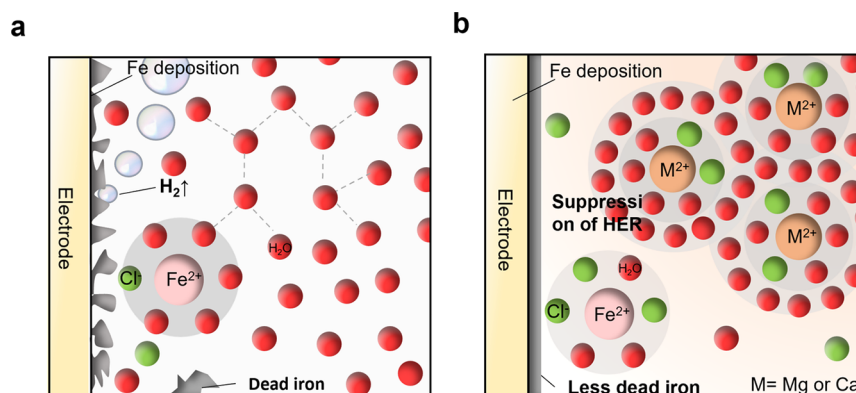

Figure 8. Schematic of (a) the structure of pure Fe electrolyte and (b) the structure of FERMI and FERCI. The improved CE is due to the suppression of HER and less dead Fe.

reduction potential of the central H_2O in a five-H_2O cluster as the reference, the reduction potentials of the central H_2O in the three-H_2O clusters were found to be −0.565, −0.654, and −0.544 V for 2A0D, 1A1D, and 0A2D, respectively. The conducted DFT calculations demonstrate that (1) the presence of Mg^{2+} and Ca^{2+} makes water more reduction resistant, and (2) decreasing the number of H-bonds that water participates in also makes water molecules more reduction resistant.

Based on the above experimental results, the enhanced CE in FERMI and FERCI can be attributed to two reasons (Figure 8). The first is less dead Fe during the stripping process. The

presence of Mg^{2+}/Ca^{2+} leads to Fe deposition with larger particle size and smaller surface area, which tends to form less dead Fe during stripping. The second is the suppression of HER because water molecules become more reduction resistant. The combined experimental and computational study suggests that the enhanced water stability toward reduction is because (1) water molecules are tightly bound by Mg^{2+}/Ca^{2+} in their hydration shells; (2) Mg^{2+}/Ca^{2+} significantly disrupts the H-bond network of water by reducing the number of H-bonds per water and increasing H-bond length, therefore strengthening the covalent O−H bond of the water molecules;[41] and (3) the reduced water concentration

results in fewer water molecules in the hydration shell of Fe^{2+}, which lowers the chance of water reduction when Fe^{2+} is brought to the electrode for Fe deposition.[42]

In addition to the remarkable enhancement of CE for Fe deposition/stripping, this study also reveals several interesting discoveries whose understanding could benefit the development of aqueous electrolytes for electrochemical technologies. An increase of the concentration of $FeCl_2$ alone from 0.5 to 3.0 M can increase the CE from 0% to 79.4% (at pH = 1). Theoretically, the addition of more Fe salts to the Fe electrolyte in the water-in-salt regime could further stabilize water and enhance the CE, as demonstrated in Zn electrolytes[36] and Li electrolytes.[37] However, the limited solubility of common Fe salts ($FeCl_2$: 3.57 M, $FeSO_4$: 3.0 M) makes it impossible to explore this regime of Fe electrolytes. This challenge may be tackled with highly water-soluble salts based on organic anions such as bis(trifluoromethanesulfonyl)imide ($TFSI^-$). The presence of a high concentration of Cl^- can enhance Fe deposition/stripping CE in electrolytes with NH_4^+,[14] but this appears only as a surface effect. This is because Cl^- can preferentially adsorb on the Fe electrode[17,37] but imposes a relatively smaller perturbation on the water structure.[23,43] Such surface effects of Cl^- are dwarfed by the bulk electrolyte structure change when cations like Na^+, Mg^{2+}, and Ca^{2+} are added due to their strong ability to bound water.[23] Because Na^+ can also reduce the number of water molecules in the hydration shell of Fe^{2+} and disrupt the water structure,[43] the addition of Na^+ to FE also enhances the CE (Figure 1f), albeit to a lesser extent compared to Mg^{2+} and Ca^{2+}. Such supremacy of Mg^{2+} and Ca^{2+} over the monovalent Na^+ is linked to their stronger ability to bind water and their ability to perturb unoccupied molecular orbitals of hydration water.[23] Between Mg^{2+} and Ca^{2+}, Ca^{2+} is slightly less effective than Mg^{2+} in enhancing the CE, which can be explained by its slightly weaker hydration than Mg^{2+} and its lesser extent of perturbing the hydration water orbital.[23,25] The effect of Mg^{2+} and Ca^{2+} in suppressing HER seems universal, as our preliminary results show that they can also enhance Zn deposition/stripping efficiency, but this discussion is beyond the scope of this work and will be presented in a future publication. Lastly, when the proposed electrolytes are used in an Fe metal battery with an intercalation cathode, such as the Prussian blue analogue,[6] Mg^{2+} or Ca^{2+} can also insert into the cathode. The selectivity of the intercalation reaction toward the alkaline earth metal ion and Fe^{2+} requires further investigation, which is beyond the scope of this work. However, this is not a concern for Fe metal flow batteries, in which charge/discharge involves electron transfer from/to the soluble redox-active ions or molecules.

To further increase the efficiency, many possible strategies can be adopted.[44] One can introduce some surface film-forming components (additives, cosalts, or cosolvents) into the aqueous electrolyte. This method is widely used in aqueous Li-ion batteries[37,45] and Zn-ion batteries.[46,47] The irreversible decomposition of these components may form an Fe^{2+} conductive but electron-insulating film (termed solid-electrolyte interphase, SEI), which allows the deposition of Fe but prevents further decomposition of water, therefore improving the efficiency. Another strategy is to suppress HER by reducing the water concentration, which can be done by further increasing the salt concentration or adding an organic solvent.[48] HER can also be suppressed by increasing the HER overpotential, which can be achieved by introducing

anticatalysts such as Bi onto the Fe metal electrode. In addition, the morphology of the Fe deposits can be further improved by adding surface surfactants to reduce the amount of dead Fe.

Safety Statement. No unexpected or unusually high safety hazards were encountered.

CONCLUSION

In conclusion, electrolytes that can support highly reversible Fe metal anode are critical to realizing the potential of aqueous Fe metal batteries as a low-cost energy storage technology. Two novel aqueous electrolytes, FERMI and FERCI, are reported in this work, and they show remarkably better Fe deposition/stripping efficiency (99.1%), higher conductivity, and lower overpotential than the baseline Fe electrolytes. Both half-cell and full-cell studies show that batteries with the baseline Fe electrolyte fail very quickly because the HER leads to large internal resistance, whereas batteries with FERMI and FERCI show significantly better cycling stability, which demonstrates the potential of these electrolytes for realizing long-cycle Fe metal batteries. Comprehensive experimental and computational studies reveal that the enhanced Fe deposition/stripping efficiency is due to a synergy of improved deposit morphology (therefore less dead Fe) and enhanced water reduction resistance. Due to the simple fabrication method and low cost of raw materials, these novel electrolytes are ideal for unleashing the low-cost benefit of Fe metal batteries, especially Fe flow batteries. Broadly, the novel electrolytes reported here not only enable long-cycle Fe metal batteries but also open a new avenue to address the HER side reaction for other electrochemical technologies based on aqueous electrolytes, such as the CO_2 reduction, NH_3 synthesis, etc.

ASSOCIATED CONTENT

ⓢ Supporting Information

The Supporting Information is available free of charge at https://pubs.acs.org/doi/10.1021/acscentsci.2c00293.

> Experimental details, SEM images, cycling performance, and electrochemical property measurements (PDF)

AUTHOR INFORMATION

Corresponding Authors

Tao Gao — *Department of Chemical Engineering, University of Utah, Salt Lake City, Utah 84114, United States;* ⓞ orcid.org/0000-0003-0204-3269; Email: taogao@chemeng.utah.edu

Dimitry Bedrov — *Department of Material Science and Engineering, University of Utah, Salt Lake City, Utah 84114, United States;* ⓞ orcid.org/0000-0002-3884-3308; Email: d.bedrov@utah.edu

Authors

Jing Liu — *Department of Chemical Engineering, University of Utah, Salt Lake City, Utah 84114, United States*

Dengpan Dong — *Department of Material Science and Engineering, University of Utah, Salt Lake City, Utah 84114, United States;* Present Address: Chemical Sciences Division, Oak Ridge National Laboratory, Oak Ridge, Tennessee 37831-6119 United States; ⓞ orcid.org/0000-0002-3381-3425

Alan Larrea Caro − *Department of Chemical Engineering, University of Utah, Salt Lake City, Utah 84114, United States*

Nicolai Sage Andreas − *Department of Chemical Engineering, University of Utah, Salt Lake City, Utah 84114, United States*

Zongjian Li − *Department of Chemical Engineering, University of Utah, Salt Lake City, Utah 84114, United States*

Yunan Qin − *Department of Chemical Engineering, University of Utah, Salt Lake City, Utah 84114, United States*

Complete contact information is available at:
https://pubs.acs.org/10.1021/acscentsci.2c00293

Notes

The authors declare no competing financial interest.

■ REFERENCES

(1) Darling, R. M.; Gallagher, K. G.; Kowalski, J. A.; Ha, S.; Brushett, F. R. Pathways to Low-Cost Electrochemical Energy Storage: A Comparison of Aqueous and Nonaqueous Flow Batteries. *Energy Environ. Sci.* **2014**, *7* (11), 3459−3477.

(2) Yang, B.; Murali, A.; Nirmalchandar, A.; Jayathilake, B.; Prakash, G. K. S.; Narayanan, S. R. A Durable, Inexpensive and Scalable Redox Flow Battery Based on Iron Sulfate and Anthraquinone Disulfonic Acid. *J. Electrochem. Soc.* **2020**, *167* (6), No. 060520.

(3) Manohar, A. K.; Kim, K. M.; Plichta, E.; Hendrickson, M.; Rawlings, S.; Narayanan, S. R. A High Efficiency Iron-Chloride Redox Flow Battery for Large-Scale Energy Storage. *J. Electrochem. Soc.* **2016**, *163* (1), A5118−A5125.

(4) Bamgbopa, M. O.; Shao-Horn, Y.; Hashaikeh, R.; Almheiri, S. Cyclable Membraneless Redox Flow Batteries Based on Immiscible Liquid Electrolytes: Demonstration with All-Iron Redox Chemistry. *Electrochim. Acta* **2018**, *267*, 41−50.

(5) Gong, K.; Xu, F.; Grunewald, J. B.; Ma, X.; Zhao, Y.; Gu, S.; Yan, Y. All-Soluble All-Iron Aqueous Redox-Flow Battery. *ACS Energy Lett.* **2016**, *1* (1), 89−93.

(6) Wu, X.; Markir, A.; Xu, Y.; Zhang, C.; Leonard, D. P.; Shin, W.; Ji, X. A Rechargeable Battery with an Iron Metal Anode. *Adv. Funct. Mater.* **2019**, *29* (20), 1900911.

(7) *Metalprices. Stainless Steel metal prices, news, charts and historical prices.* https://www.metalary.com/ (accessed 2022−03 −06).

(8) He, Z.; Xiong, F.; Tan, S.; Yao, X.; Zhang, C.; An, Q. Iron Metal Anode for Aqueous Rechargeable Batteries. *Mater. Today Adv.* **2021**, *11*, 100156.

(9) Xu, Y.; Wu, X.; Sandstrom, S. K.; Hong, J. J.; Jiang, H.; Chen, X.; Ji, X. Fe-Ion Bolted VOPO₄ •2H₂O as an Aqueous Fe-Ion Battery Electrode. *Adv. Mater.* **2021**, *33*, 2105234.

(10) Shukla, A. K.; Ravikumar, M. K.; Balasubramanian, T. S. Nickel/Iron Batteries. *J. Power Sources* **1994**, *51* (1−2), 29−36.

(11) Yu, S.; Yue, X.; Holoubek, J.; Xing, X.; Pan, E.; Pascal, T.; Liu, P. A Low-Cost Sulfate-Based All Iron Redox Flow Battery. *J. Power Sources* **2021**, *513* (April), 230457.

(12) Pentland, N.; Bockris, J. O.; Sheldon, E. Hydrogen Evolution Reaction on Copper, Gold, Molybdenum, Palladium, Rhodium, and Iron. *J. Electrochem. Soc.* **1957**, *104* (3), 182.

(13) Jayathilake, B. S.; Plichta, E. J.; Hendrickson, M. A.; Narayanan, S. R. Improvements to the Coulombic Efficiency of the Iron Electrode for an All-Iron Redox-Flow Battery. *J. Electrochem. Soc.* **2018**, *165* (9), A1630−A1638.

(14) Hawthorne, K. L.; Petek, T. J.; Miller, M. A.; Wainright, J. S.; Savinell, R. F. An Investigation into Factors Affecting the Iron Plating Reaction for an All-Iron Flow Battery. *J. Electrochem. Soc.* **2015**, *162* (1), A108−A113.

(15) Noack, J.; Berkers, M.; Ortner, J.; Pinkwart, K. The Influence of Some Electrolyte Additives on the Electrochemical Performance of Fe/Fe 2+ Redox Reactions for Iron/Iron Redox Flow Batteries. *J. Electrochem. Soc.* **2021**, *168* (4), No. 040529.

(16) Jeyaprabha, C.; Sathiyanarayanan, S.; Muralidharan, S.; Venkatachari, G.; Jeyaprabha, C.; Sathiyanarayanan, S.; Muralidharan, S.; Venkatachari, G. Corrosion inhibition of iron in 0.5 mol L-1 H2SO4 by halide ions. *J. Braz. Chem. Soc.* **2006**, *17* (1), 61−67.

(17) Elhamid, M. H. A.; Ateya, B. G.; Pickering, H. W. The Effect of Iodide Ions on the Kinetics of Hydrogen Absorption by Iron. *J. Electrochem. Soc.* **2000**, *147* (6), 2258.

(18) Beverskog, B.; Puigdomenech, I. Revised Pourbaix Diagrams for Iron At 25−300° C. *Corrosion Science* **1996**, *38* (12), 2121−2135.

(19) Kim, G.-T.; Appetecchi, G. B.; Montanino, M.; Alessandrini, F.; Passerini, S. (Invited) Long-Term Cyclability of Lithium Metal Electrodes in Ionic Liquid-Based Electrolytes at Room Temperature. *ECS Trans.* **2010**, *25* (36), 127−138.

(20) Kear, G.; Barker, B. D.; Walsh, F. C. Electrochemical Corrosion of Unalloyed Copper in Chloride Media–a Critical Review. *Corros. Sci.* **2004**, *46* (1), 109−135.

(21) Fang, C.; Li, J.; Zhang, M.; Zhang, Y.; Yang, F.; Lee, J. Z.; Lee, M. H.; Alvarado, J.; Schroeder, M. A.; Yang, Y.; Lu, B.; Williams, N.; Ceja, M.; Yang, L.; Cai, M.; Gu, J.; Xu, K.; Wang, X.; Meng, Y. S. Quantifying Inactive Lithium in Lithium Metal Batteries. *Nature* **2019**, *572* (7770), 511−515.

(22) Zhang, J. G.; Xu, W.; Xiao, J.; Cao, X.; Liu, J. Lithium Metal Anodes with Nonaqueous Electrolytes. *Chem. Rev.* **2020**, *120* (24), 13312−13348.

(23) Cappa, C. D.; Smith, J. D.; Messer, B. M.; Cohen, R. C.; Saykally, R. J. Effects of Cations on the Hydrogen Bond Network of Liquid Water: New Results from x-Ray Absorption Spectroscopy of Liquid Microjets. *J. Phys. Chem. B* **2006**, *110* (11), 5301−5309.

(24) Sun, Q. The Raman OH Stretching Bands of Liquid Water. *Vib. Spectrosc.* **2009**, *51* (2), 213−217.

(25) Friesen, S.; Hefter, G.; Buchner, R. Cation Hydration and Ion Pairing in Aqueous Solutions of MgCl 2 and CaCl 2. *J. Phys. Chem. B* **2019**, *123* (4), 891−900.

(26) Pavlov, M.; Siegbahn, P. E. M.; Sandström, M. Hydration of Beryllium, Magnesium, Calcium, and Zinc Ions Using Density Functional Theory. *J. Phys. Chem. A* **1998**, *102* (1), 219−228.

(27) Roy, S.; Patra, A.; Saha, S.; Palit, D. K.; Mondal, J. A. Restructuring of Hydration Shell Water Due to Solvent-Shared Ion Pairing (SSIP): A Case Study of Aqueous MgCl2and LaCl3Solutions. *J. Phys. Chem. B* **2020**, *124* (37), 8141−8148.

(28) Li, R.; Jiang, Z.; Shi, S.; Yang, H. Raman Spectra and 17O NMR Study Effects of CaCl2 and MgCl2 on Water Structure. *J. Mol. Struct.* **2003**, *645* (1), 69−75.

(29) Kanno, H.; Hiraishi, J. A Raman Study of Aqueous Solutions of Ferric Nitrate, Ferrous Chloride and Ferric Chloride in the Glassy State. *J. Raman Spectrosc.* **1982**, *12* (3), 224−227.

(30) Zhang, C.; Holoubek, J.; Wu, X.; Daniyar, A.; Zhu, L.; Chen, C.; Leonard, D. P.; Rodríguez-Pérez, I. A.; Jiang, J. X.; Fang, C.; Ji, X.

A ZnCl2 Water-in-Salt Electrolyte for a Reversible Zn Metal Anode. *Chem. Commun.* **2018**, *54* (100), 14097−14099.

(31) Borodin, O. Polarizable Force Field Development and Molecular Dynamics Simulations of Ionic Liquids. *J. Phys. Chem. B* **2009**, *113* (33), 11463−11478.

(32) Bedrov, D.; Piquemal, J. P.; Borodin, O.; MacKerell, A. D.; Roux, B.; Schröder, C. Molecular Dynamics Simulations of Ionic Liquids and Electrolytes Using Polarizable Force Fields. *Chem. Rev.* **2019**, *119* (13), 7940−7995.

(33) Henchman, R. H.; Irudayam, S. J. Topological Hydrogen-Bond Definition to Characterize the Structure and Dynamics of Liquid Water. *J. Phys. Chem. B* **2010**, *114* (50), 16792−16810.

(34) Grabowski, S. J. A New Measure of Hydrogen Bonding Strength - Ab Initio and Atoms in Molecules Studies. *Chem. Phys. Lett.* **2001**, *338* (4−6), 361−366.

(35) Chaplin, M. F. Water's Hydrogen Bond Strength. In *Water and Life: The Unique Properties of H₂O*; Lynden-Bell, R. M., Ed.; CRC Press: Boca Raton, FL, 2010; pp 69−86..

(36) Zhang, C.; Holoubek, J.; Wu, X.; Daniyar, A.; Zhu, L.; Chen, C.; Leonard, D. P.; Rodríguez-Pérez, I. A.; Jiang, J. X.; Fang, C.; Ji, X. A ZnCl2 Water-in-Salt Electrolyte for a Reversible Zn Metal Anode. *Chem. Commun.* **2018**, *54* (100), 14097−14099.

(37) Suo, L.; Borodin, O.; Gao, T.; Olguin, M.; Ho, J.; Fan, X.; Luo, C.; Wang, C.; Xu, K. Water-in-Salt" Electrolyte Enables High-Voltage Aqueous Lithium-Ion Chemistries. *Science (80-.).* **2015**, *350* (6263), 938−943.

(38) Rossmeisl, J.; Chan, K.; Ahmed, R.; Tripković, V.; Björketun, M. E. PH in Atomic Scale Simulations of Electrochemical Interfaces. *Phys. Chem. Chem. Phys.* **2013**, *15* (25), 10321−10325.

(39) Borodin, O.; Olguin, M.; Spear, C. E.; Leiter, K. W.; Knap, J. Towards High Throughput Screening of Electrochemical Stability of Battery Electrolytes. *Nanotechnology* **2015**, *26* (35), 354003.

(40) Delp, S. A.; Borodin, O.; Olguin, M.; Eisner, C. G.; Allen, J. L.; Jow, T. R. Importance of Reduction and Oxidation Stability of High Voltage Electrolytes and Additives. *Electrochim. Acta* **2016**, *209*, 498−510.

(41) Ji, X. A Perspective of ZnCl2 Electrolytes: The Physical and Electrochemical Properties. *eScience* **2021**, *1* (2), 99−107.

(42) Zhang, C.; Shin, W.; Zhu, L.; Chen, C.; Neuefeind, J. C.; Xu, Y.; Allec, S. I.; Liu, C.; Wei, Z.; Daniyar, A.; Jiang, J. X.; Fang, C.; Alex Greaney, P.; Ji, X. The Electrolyte Comprising More Robust Water and Superhalides Transforms Zn-Metal Anode Reversibly and Dendrite-Free. *Carbon Energy* **2021**, *3* (2), 339−348.

(43) Mancinelli, R.; Botti, A.; Bruni, F.; Ricci, M. A.; Soper, A. K. Hydration of Sodium, Potassium, and Chloride Ions in Solution and the Concept of Structure Maker/Breaker. *J. Phys. Chem. B* **2007**, *111* (48), 13570−13577.

(44) Sui, Y.; Ji, X. Anticatalytic Strategies to Suppress Water Electrolysis in Aqueous Batteries. *Chem. Rev.* **2021**, *121* (11), 6654−6695.

(45) Suo, L.; Oh, D.; Lin, Y.; Zhuo, Z.; Borodin, O.; Gao, T.; Wang, F.; Kushima, A.; Wang, Z.; Kim, H. C.; Qi, Y.; Yang, W.; Pan, F.; Li, J.; Xu, K.; Wang, C. How Solid-Electrolyte Interphase Forms in Aqueous Electrolytes. *J. Am. Chem. Soc.* **2017**, *139* (51), 18670−18680.

(46) Li, D.; Cao, L.; Deng, T.; Liu, S.; Wang, C. Design of a Solid Electrolyte Interphase for Aqueous Zn Batteries. *Angew. Chem., Int. Ed. Engl.* **2021**, *60* (23), 13035−13041.

(47) Zeng, X.; Mao, J.; Hao, J.; Liu, J.; Liu, S.; Wang, Z.; Wang, Y.; Zhang, S.; Zheng, T.; Liu, J.; Rao, P.; Guo, Z. Electrolyte Design for In Situ Construction of Highly Zn2+-Conductive Solid Electrolyte Interphase to Enable High-Performance Aqueous Zn-Ion Batteries under Practical Conditions. *Adv. Mater.* **2021**, *33* (11), 2007416.

(48) Yokoyama, Y.; Fukutsuka, T.; Miyazaki, K.; Abe, T. Origin of the Electrochemical Stability of Aqueous Concentrated Electrolyte Solutions. *J. Electrochem. Soc.* **2018**, *165* (14), A3299−A3303.